Bifurcation structure of periodic patterns in the Lugiato-Lefever equation with anomalous dispersion

P. Parra-Rivas,[1,2,3] D. Gomila,[3] L. Gelens,[1,2] and E. Knobloch[4]

[1]*Laboratory of Dynamics in Biological Systems, KU Leuven Department of Cellular and Molecular Medicine, University of Leuven, B-3000 Leuven, Belgium*

[2]*Applied Physics Research Group, APHY, Vrije Universiteit Brussel, 1050 Brussels, Belgium*

[3]*Instituto de Física Interdisciplinar y Sistemas Complejos, IFISC (CSIC-UIB), Campus Universitat de les Illes Balears, E-07122 Palma de Mallorca, Spain*

[4]*Department of Physics, University of California, Berkeley, California 94720, USA*

(Received 4 May 2018; published 18 October 2018)

We study the stability and bifurcation structure of spatially extended patterns arising in nonlinear optical resonators with a Kerr-type nonlinearity and anomalous group velocity dispersion, as described by the Lugiato-Lefever equation. While there exists a one-parameter family of patterns with different wavelengths, we focus our attention on the pattern with critical wave number k_c arising from the modulational instability of the homogeneous state. We find that the branch of solutions associated with this pattern connects to a branch of patterns with wave number $2k_c$. This next branch also connects to a branch of patterns with double wave number, this time $4k_c$, and this process repeats through a series of 2:1 spatial resonances. For values of the detuning parameter approaching $\theta = 2$ from below the critical wave number k_c approaches zero and this bifurcation structure is related to the foliated snaking bifurcation structure organizing spatially localized bright solitons. Secondary bifurcations that these patterns undergo and the resulting temporal dynamics are also studied.

DOI: 10.1103/PhysRevE.98.042212

I. INTRODUCTION

Since the formulation in 1987 of the Lugiato-Lefever (LL) model describing light propagation in nonlinear optical Kerr cavities [1], the existence and origin of spatially extended patterned solutions has been widely studied in both temporal and spatial systems [2–7]. In the LL model, it was shown that patterns arise through a Turing instability, usually referred to as a modulational instability (MI) in the optics context [8–11]. In this type of instability a homogeneous steady state (HSS) becomes unstable to perturbations with a given wavelength, which then further develops into an ordered modulated structure: a *pattern*.

In recent years, dissipative structures arising in the one-dimensional LL model have been studied extensively because of their intimate connection to frequency combs in microresonators driven by a continuous wave laser [6,12,13]. Such frequency combs correspond to the frequency spectrum of localized or extended light patterns that circulate inside the cavity [14–18], and can be used for a wide variety of applications [19]. In this work, we study the stability and bifurcation structure of extended patterns in the LL model,

$$\partial_t A = -(1 + i\theta)A + i\nu\partial_x^2 A + i|A|^2 A + \rho, \qquad (1)$$

where ρ and θ are real control parameters representing normalized energy injection and frequency detuning, respectively. We focus here on the anomalous group velocity dispersion (GVD) regime and therefore set $\nu = 1$ throughout this work. We study patterns with the critical wave number k_c introduced below, originating from the modulational instability. For the parameter values for which the patterns are subcritical, this bifurcation also leads to the formation of localized structures. For a detailed study of the bifurcation structure of such localized states in the LL model, we refer to [20].

This paper is organized as follows. In Sec. II, we perform the linear stability analysis of the HSS solution with respect to spatially periodic perturbations. This not only reveals the modulational instability, but more generally indicates which perturbation wave numbers lead to instabilities and pattern formation. Next, in Sec. III, we show how analytical expressions for weakly nonlinear pattern solutions can be found near certain bifurcations. Next, in Sec. IV, we numerically track these analytical solutions to values of the pump parameter ρ away from the bifurcation points, thus revealing the bifurcation structure of the patterns for a fixed value of the detuning. In Sec. V we study how this bifurcation structure changes as the parameter space defined by the cavity detuning θ and the pump ρ is traversed, and present phase diagrams showing parameter regimes with distinct pattern behavior. In Sec. VI a linear stability analysis of the pattern solutions is performed, and the different secondary instabilities that these states undergo are discussed. Finally, in Sec. VII we give some concluding remarks.

II. LINEAR STABILITY ANALYSIS OF THE HOMOGENEOUS STEADY STATES

The HSS solutions A_0 can be found by solving the classic cubic equation of dispersive optical bistability, namely

$$I_0^3 - 2\theta I_0^2 + (1 + \theta^2)I_0 = \rho^2, \qquad (2)$$

where $I_0 \equiv |A_0|^2$. The solutions in real variables ($U_0 = \mathrm{Re}[A_0]$, $V_0 = \mathrm{Im}[A_0]$) are given by

$$\begin{bmatrix} U_0 \\ V_0 \end{bmatrix} = \begin{bmatrix} \dfrac{\rho}{1+(I_0-\theta)^2} \\ \dfrac{(I_0-\theta)\rho}{1+(I_0-\theta)^2} \end{bmatrix}. \tag{3}$$

For $\theta < \sqrt{3}$, Eq. (2) is single valued and hence the system is monostable. In contrast, for $\theta > \sqrt{3}$, Eq. (2) is triple valued. The transition between the three different solutions occurs via a pair of saddle-node bifurcations SN_b and SN_t located at

$$I_{t,b} \equiv |A_{t,b}|^2 = \frac{2\theta}{3} \pm \frac{1}{3}\sqrt{\theta^2 - 3}, \tag{4}$$

and these arise from a cusp or hysteresis bifurcation at $\theta = \sqrt{3}$. In what follows, we denote the bottom solution branch (from $I_0 = 0$ to I_b) by A_0^b, the middle branch between I_b and I_t by A_0^m, and the top branch by A_0^t ($I_0 > I_t$).

A linear stability analysis of the HSS solution with respect to spatially periodic perturbations of the form

$$\begin{bmatrix} U \\ V \end{bmatrix} = \begin{bmatrix} U_0 \\ V_0 \end{bmatrix} + \epsilon \begin{bmatrix} u_1(x,t) \\ v_1(x,t) \end{bmatrix} + O(\epsilon^2), \tag{5}$$

where $|\epsilon| \ll 1$ and

$$\begin{bmatrix} u_1 \\ v_1 \end{bmatrix} = \begin{bmatrix} a_k \\ b_k \end{bmatrix} e^{ikx+\Omega t} + \text{c.c.}, \tag{6}$$

leads to the dispersion relation

$$\Omega(k) = -1 \pm \sqrt{4I_0\theta - 3I_0^2 - \theta^2 + (4I_0 - 2\theta)k^2 - k^4}. \tag{7}$$

Here $\Omega(k)$ is the linear growth rate of a perturbation with wave number k.

In the linear approximation, the superposition principle applies and therefore any pattern solution of the problem can be written as the linear combination

$$\begin{bmatrix} u_1 \\ v_1 \end{bmatrix}_{(x,t)} = \sum_k \begin{bmatrix} a_k \\ b_k \end{bmatrix} e^{ikx+\Omega t} + \text{c.c.}, \tag{8}$$

where the mode amplitudes a_k, b_k depend on the parameters θ and ρ. The growth rate $\Omega(k)$ will in general be positive for wave numbers within an interval $[k^-, k^+]$, where the wave numbers k^- and k^+ depend on I_0 and solve the quadratic equation

$$k^4 - (4I_0 - 2\theta)k^2 + 3I_0^2 + \theta^2 - 4I_0\theta + 1 = 0. \tag{9}$$

Any mode within this interval will grow, and the profile of a pattern arising from random noise will be dominated by the most unstable mode k_u defined by the condition $\Omega'(k_u) \equiv \frac{d\Omega}{dk}|_{k_u} = 0$, giving

$$k_u = \sqrt{2I_0 - \theta}. \tag{10}$$

The loss of stability occurs at a critical value of k_c where the growth rate first reaches zero, i.e., when conditions (9) and (10) are satisfied simultaneously. This transition is called a Turing [8–11] or modulational instability (MI), and occurs at $I_0 = I_c$, $k = k_c$, where

$$I_c = 1, \quad k_c = \sqrt{2-\theta}. \tag{11}$$

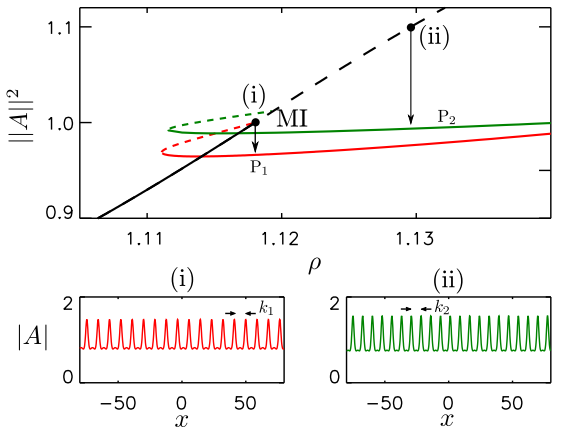

FIG. 1. Stable HSS (black solid line) is destabilized at the modulational instability MI. Close to MI (i) the unstable HSS evolves to the pattern branch P_1 (red) consisting of stationary patterns with wave number $k_1 = 0.706849 \approx k_c = 0.707107$. Further away from MI (ii) the unstable HSS evolves into a different pattern branch P_2 (green), associated with patterns with wave number $k_2 = 0.824564 \approx k_u = 0.836642$. Stable (unstable) solutions are denoted by solid (dashed) lines. Here $\theta = 1.5$ and $L = 160$.

Evidently, this transition is only found when $\theta < 2$. The condition $I_0 = I_c$ defines a line in the parameter space (θ, ρ) given by

$$\rho_c = \sqrt{1 + (1-\theta)^2}. \tag{12}$$

Figure 1 illustrates how the HSS destabilizes when the pump parameter ρ exceeds $\rho = \rho_c$ and how the pattern state is subsequently reached. The wave number of this pattern changes with the pump parameter as does the most unstable wave number [see Eq. (10)]. Close to the MI the HSS develops into a pattern that lies on a branch of pattern solutions with wave number close to k_c, originating near MI. For larger values of the pump, however, the selected pattern belongs to a pattern branch corresponding to a wave number close to the fastest growing wave number k_u. This observation highlights the fact that the pattern branches form a continuum, parametrized by the wave number $k \in [k^-, k^+]$, with the wave number selected by nonlinear processes that depend on the system parameters. In this work we restrict attention to pattern branches corresponding to the critical wave number k_c and its harmonics, and describe their bifurcation structure in some detail. The study of patterns with other wave numbers is left for future work.

Before turning to the bifurcation structure of pattern solutions, we start our analysis by studying the set of points k^- and k^+ satisfying Eq. (9). These points define the so-called *marginal stability curve* defined by

$$\mathrm{I}_k^{\pm}(\theta) = \frac{2}{3}(\theta + k^2) \pm \frac{1}{3}\sqrt{\theta^2 + k^4 + 2\theta k^2 - 3}. \tag{13}$$

The marginal stability curves are shown in the panels on the left of Fig. 2 for increasing values of the detuning θ. The HSS solutions at the corresponding values of θ are shown in the panels on the right, with solid (dashed) lines representing the HSS solutions that are stable (unstable) against perturbations of the form (6). For a fixed value of θ, and for a given

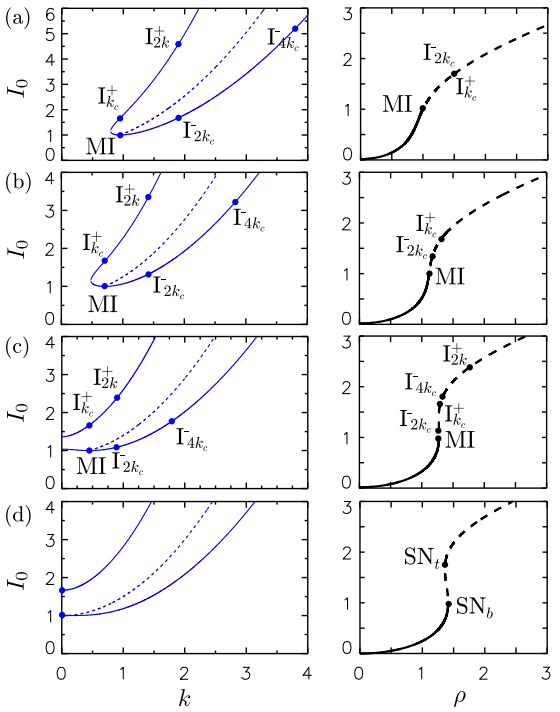

FIG. 2. Left: marginal instability curves for (a) $\theta = 1.1$, (b) $\theta = 1.5$, (c) $\theta = 1.8$, and (d) $\theta = 2.0$. Right: the HSS solutions corresponding to the same values of θ. Solid (dashed) lines represent stable (unstable) HSSs with respect to perturbations of the form (6). The locations $\mathrm{I}^{\pm}_k$ corresponding to instabilities with wave number k are indicated using solid circles. The dashed line inside the marginal instability curves in the left panels represents the most unstable mode $k = k_u$.

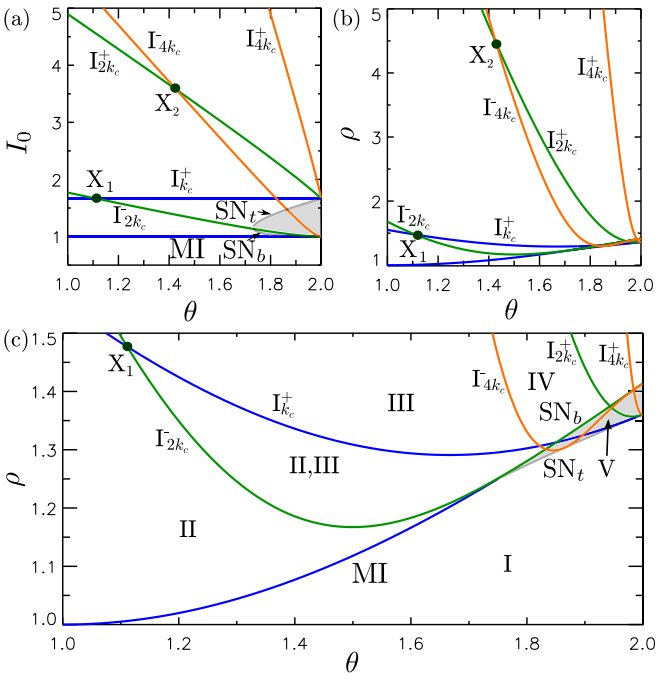

FIG. 3. (a) Instability lines $\mathrm{I}^{\pm}_{k_c}$ and the location of the saddle-node bifurcations of the HSSs in the parameter space (θ, I_0). (b) Same as (a) but in the parameter space (θ, ρ). (c) Zoom of (b) showing the main regions with distinct bifurcation behavior (see text). The labels X_1 and X_2 indicate codimension-two points. In both (a) and (c) the gray area represents region V where the HSS is triple valued.

wave number k', the HSS solution is unstable if $\mathrm{I}^-_{k'}(\theta) < I_0 < \mathrm{I}^+_{k'}(\theta)$ and stable otherwise. Thus, for a given wave number $k = k_c$ a pattern P_{k_c} bifurcates from the points $\mathrm{I}^{\pm}_{k_c}(\theta)$ indicated in Fig. 2 and similarly for patterns with wave number $2k_c$, $4k_c$, etc.

In Fig. 2(a), for $\theta = 1.1$, the HSS is always stable against perturbations with $k = 0$. Furthermore, a pattern with wave number k_c bifurcates from the MI at $\mathrm{I}^-_{k_c} = \mathrm{I}_c$ and then reconnects with HSS again at $\mathrm{I}^+_{k_c} > \mathrm{I}^-_{k_c}$. Similarly, a pattern with $2k_c$ arises initially from $\mathrm{I}^-_{2k_c}$ and reconnects to HSS at $\mathrm{I}^+_{2k_c}$. The situation for all subsequent harmonics is similar. As the detuning θ increases, the different instability points for modes with $k = k_c$ and its harmonics approach each other as the whole tongue of unstable modes shifts to lower values of k [see Fig. 2(b)]. This behavior can also be seen in Fig. 3 where we plot the instability boundaries in the parameter space (θ, I_0) and (θ, ρ), respectively, together with the location of the saddle-node bifurcations SN_b and SN_t of the HSS solution. For $\theta < \sqrt{3}$, A_0 is always stable against spatially uniform perturbations with $k = 0$. In contrast, when $\sqrt{3} < \theta < 2$, the response of the HSSs as a function of the pump parameter ρ becomes bistable. In this case, the bottom A^b_0 and top A^t_0 branches are stable with respect to $k = 0$ perturbations, while the middle branch A^m_0 is unstable to such perturbations. However, A^t_0 and A^m_0 are always unstable with respect to $k > 0$ perturbations, while A^b_0 is only destabilized above $I_0 = I_c$. This situation is depicted in Fig. 2(c) for $\theta = 1.8$, where the tongue of unstable wave numbers now starts at $k = 0$.

Finally, when the detuning increases to $\theta = 2$ from below, the instability points $\mathrm{I}^{\pm}_{nk_c}$, $n = 1, 2, \ldots$, approach one another until they all collapse at $k = 0$ and the MI disappears [see Fig. 2(d)]. A similar collapse can be seen in Fig. 3, where $\mathrm{I}^+_{k_c}$ and $\mathrm{I}^-_{2k_c}$, and $\mathrm{I}^+_{2k_c}$ and $\mathrm{I}^-_{4k_c}$ collide pairwise at the codimension-two bifurcation X_1 and X_2 located at $(\theta_{\mathrm{X}_1}, \rho_{\mathrm{X}_1}) = (1.1111, 1.4768)$ and $(\theta_{\mathrm{X}_2}, \rho_{\mathrm{X}_2}) = (1.4286, 4.468)$, respectively. The results presented in Fig. 2 and Fig. 3 are limited to $\theta < 2$ for which the MI exists and takes place at $I_0 = I_c$. When approaching $\theta = 2$ from below, the critical wave number approaches zero ($k_c \to 0$), implying that the wavelength of the nascent pattern diverges. In this context a single peak in a periodic domain can be thought of as one wavelength of a periodic array of peaks parametrized by the domain period L. As the wavelength of the pattern diverges to infinity so does L and the distinction between patterns and localized structures becomes blurred [20]. A detailed analysis of how the bifurcation structure of such localized structures changes as one approaches this critical point $\theta = 2$ can be found in Ref. [20].

At this point we can already identify several distinct solution regimes based on the existence of patterns and the stability of A_0 as follows.

Region I: the HSS solution A_0 is stable. This region spans the parameter space $\rho < \rho_c$.

Region II: the pattern P_{k_c} exists between MI and $\mathrm{I}^+_{k_c}$, and A_0 is unstable.

Region III: the pattern P_{2k_c} exists between $I^-_{2k_c}$ and $I^+_{2k_c}$, and A_0 is unstable.

Region IV: the pattern P_{4k_c} exists between $I^-_{4k_c}$ and $I^+_{4k_c}$, and A_0 is unstable.

Region V: multistability of the HSS A_0. A_0^b is stable, while A_0^t and A_0^m are unstable. This region spans the parameter region between SN_b and SN_t. The patterns P_{k_c} and P_{2k_c} also exist in this region since they appear subcritically.

In the following sections we study how the different patterns reconnect as parameters are varied, and identify the different instabilities these patterns undergo.

III. WEAKLY NONLINEAR PATTERN SOLUTIONS

Weakly nonlinear patterns are present in the vicinity of the MI bifurcation at $I_0 = I_c$ and can be computed using multiscale perturbation analysis. At leading order in the expansion parameter ϵ, defined by the relation $\rho = \rho_c + \epsilon^2\mu$, the pattern solution is given by

$$\begin{bmatrix} U \\ V \end{bmatrix} = \begin{bmatrix} U_c \\ V_c \end{bmatrix} + \epsilon \begin{bmatrix} u_1 \\ v_1 \end{bmatrix} + \epsilon^2 \begin{bmatrix} U_2 \\ V_2 \end{bmatrix}, \tag{14}$$

where U_c and V_c correspond to the HSS solution (3) at $\rho = \rho_c$, U_2 and V_2 represent the leading order correction to this HSS, given by

$$\begin{bmatrix} U_2 \\ V_2 \end{bmatrix} = \frac{\mu}{(\theta^2 - 2\theta + 2)(\theta - 2)} \begin{bmatrix} \theta^2 \\ -\theta^2 - \theta + 2 \end{bmatrix}, \tag{15}$$

and the space-dependent correction is given by

$$\begin{bmatrix} u_1 \\ v_1 \end{bmatrix} = 2 \begin{bmatrix} a \\ 1 \end{bmatrix} B \cos(k_c x + \varphi), \tag{16}$$

where φ is an arbitrary phase and

$$a = \frac{\theta}{2 - \theta}. \tag{17}$$

The amplitude B of the pattern state corresponds to the constant solution of the amplitude equation

$$C_1 B_{XX} + \mu C_2 B + C_3 B^3 = 0, \tag{18}$$

i.e.,

$$B = \sqrt{-\mu C_2 / C_3}. \tag{19}$$

Here

$$C_1 = -\frac{2(\theta^2 - 2\theta + 2)}{\theta - 2}, \tag{20}$$

$$C_2 = \frac{2(\theta^2 - 2\theta + 2)^{\frac{3}{2}}}{(\theta - 2)^4}, \tag{21}$$

$$C_3 = \frac{4(\theta^2 - 2\theta + 2)^2(30\theta - 41)}{9(\theta - 2)^6}. \tag{22}$$

It follows that the pattern is supercritical for $\theta < 41/30$ but subcritical for $\theta > 41/30$, as already predicted in Refs. [1,21]. In the following we refer to this pattern as P_{k_c}. Details of the above calculation can be found in Ref. [20]. We have to point out that in the weakly subcritical regime (i.e., $\theta \gtrsim 41/30$) one may proceed to fifth order in the calculation in order to capture larger amplitude stable solutions. However, in our case, we are only interested in the small amplitude periodic patterns emerging from the MI bifurcation, which are well described by Eq. (18). Figure 4 shows the excellent correspondence between the analytical asymptotic solution (14) (solid blue line) and the numerically exact solution (red diamonds) of Eq. (1) obtained using numerical continuation (see Sec. IV) for both super- and subcritical patterns in this regime. Panels (a),(b) correspond to the real and imaginary parts of a supercritical pattern at $(\theta, \rho) = (1.1, 1.00499)$, while panels (c),(d) correspond to a subcritical pattern at $(\theta, \rho) = (1.5, 1.11802)$.

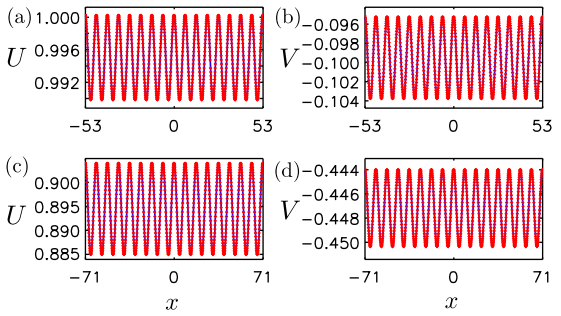

FIG. 4. Comparison between the asymptotic solution (14) (blue solid line) and the corresponding numerically exact solutions (red diamonds) obtained using a Newton-Raphson solver (see Sec. IV) for (a),(b) a supercritical pattern at $\theta = 1.1$ and (c),(d) a subcritical pattern at $\theta = 1.5$. In (a) and (c) the real part U is shown, while (b) and (d) show the imaginary part V. In both cases the numerical and analytical curves are almost indistinguishable. In both cases $L = n2\pi/k_c$, with $n = 16$, and $|\rho - \rho_c| = 10^{-5}$.

IV. BIFURCATION STRUCTURE OF PATTERNS

We now present the main features of the bifurcation structure of the pattern states for a fixed value of the detuning, choosing $\theta = 1.5$ as a representative value, leaving the study of how this structure is modified as θ varies to the following section. Starting from the analytical solution (14), valid close to the MI bifurcation, we use a numerical continuation algorithm to construct the bifurcation diagram shown in Fig. 5, showing the intensity $||A||^2$ as a function of the parameter ρ. This algorithm allows us to calculate numerically, using a Newton-Raphson solver, not only stable, but also unstable stationary periodic patterns, and to track them as a function of a suitable continuation (control) parameter [22–24]. Furthermore, the spectrum of the linearization about these patterns gives us information about their linear stability. Section VI is devoted to this analysis. As in Fig. 1, the black lines in Fig. 5 represent HSSs, while red, blue, and green lines correspond to patterned states with wave number k_c, $2k_c$, and $4k_c$, respectively. Furthermore, solid lines denote stable solutions, while dashed lines indicate unstable ones. The solution profiles along these branches, calculated numerically with these methods, are illustrated in panels (i)–(xii). As shown in Fig. 1, the pattern P_{k_c} with wave number k_c originates at the MI bifurcation.

While the MI bifurcation corresponds to the point where the HSSs lose stability to temporal perturbations, it is also possible to study this transition in the context of spatial

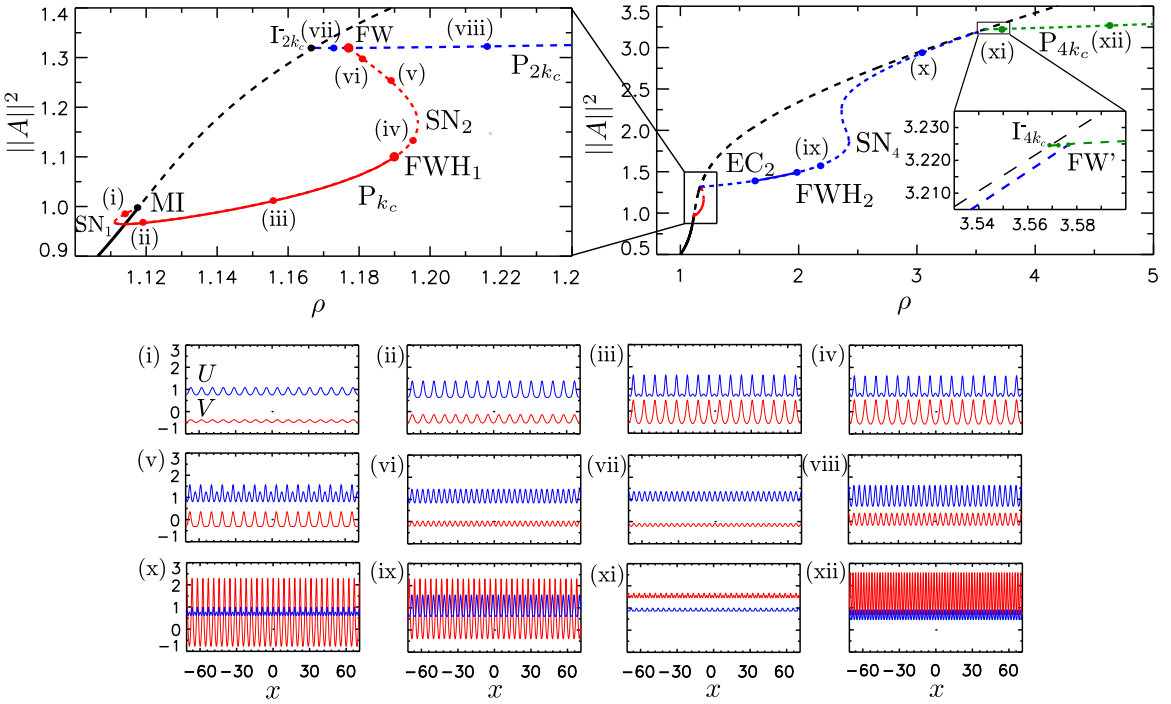

FIG. 5. Bifurcation diagrams for patterns with wave numbers k_c, $2k_c$, and $4k_c$ for $\theta = 1.5$. Solution profiles along the different branches obtained from numerical continuation are shown in panels (i)–(xii).

dynamics. Here, the HSS is interpreted as a fixed point in a four-dimensional phase space [20], and the MI corresponds to a Hamiltonian-Hopf (HH) bifurcation with eigenvalues $\lambda = \pm ik_c$ of double multiplicity. In this formulation the pattern state corresponds to a periodic orbit, and this orbit bifurcates from HSS at ρ_c (for $\theta < 2$) with initial period (wavelength) $2\pi/k_c$. Together with this critical pattern there is a continuous family of patterns with $k \in [k^-, k^+]$ that bifurcates from the HSS solution for $\rho > \rho_c$. Within the spatial dynamics framework the HSS points for $\rho > \rho_c$ are nonhyperbolic and the bifurcations to $\mathrm{P}_{2k_c}, \mathrm{P}_{4k_c}, \ldots$ have no particular signature within the spatial dynamics point of view. However, linear stability theory in the time domain shows that bifurcations occur whenever the spatial eigenvalues on the imaginary axis are in resonance, $k = nk_c$, where n is an integer. Theory also shows that the primary bifurcation to periodic orbits at ρ_c is accompanied by the simultaneous appearance of a pair of branches of spatially localized structures, provided only that the periodic states bifurcate subcritically. As a result the localized states can be interpreted as portions of the pattern state embedded in a uniform background. The bifurcation structure of such localized structures is studied in detail in Ref. [20].

As the detuning θ in Fig. 5 is larger than $41/30$, the pattern P_{k_c} is created subcritically and is therefore initially temporally unstable [see profile (i)]. Following this branch away from MI, the pattern grows in amplitude and gains stability at a saddle-node bifurcation SN_1 [profiles (ii),(iii)], but loses stability at a secondary finite-wavelength-Hopf (FWH_1) bifurcation occurring very close to the second saddle-node SN_2 [profiles (iv)–(vi)]. Such secondary instabilities are studied in detail in subsequent sections. Once SN_2 is passed, spatial oscillations (SOs) start to appear in between the peaks in the pattern profile as seen most clearly in profile (v). These SOs correspond to the growth of the second harmonic $2k_c$ of the pattern wave number, and these grow in amplitude with increasing ρ [profile (vi)] until P_{k_c} merges with the pattern P_{2k_c}, a state with wave number $2k_c$ (plus harmonics). The merging of these two periodic orbits occurs in a 2:1 spatial resonance [25–27], which in the context of patterns corresponds to a finite wavelength (FW) instability of P_{2k_c} that doubles its wavelength, i.e., to a (spatial) subharmonic instability.

The pattern P_{2k_c} itself bifurcates supercritically from HSS at $\mathrm{I}^-_{2k_c}$. Since this branch inherits the unstable eigenvalue of HSS the P_{2k_c} branch is initially unstable. The resulting pattern likewise grows in amplitude as ρ increases [profiles (vii),(viii)]. Moreover, a region of stability appears between two new secondary bifurcations: an Eckhaus bifurcation (EC_2) and the FWH_2 (see Sec. VI). At SN_4, the solution branch folds back and, just as for P_{k_c}, SOs appear between successive peaks in the profile and the pattern terminates at a FW′ point on the P_{4k_c} branch with characteristic wave number $4k_c$ once the amplitude of the SOs reaches that of the original peaks. This new pattern again bifurcates supercritically from the HSS, this time at $\mathrm{I}^-_{4k_c}$ [profile (xi)], and is likewise initially unstable before terminating in yet another 2:1 spatial resonance [profile (xii)]. We have identified a whole cascade of such bifurcations involving even higher harmonics of k_c.

Bifurcation theory sheds light on the bifurcation sequence described above. We imagine that the bifurcations to P_{k_c} and P_{2k_c} occur in close succession and so look for solutions in the form $(U, V) \propto z_1 \exp ik_c x + z_2 \exp 2ik_c x + \mathrm{c.c.} + \mathrm{h.o.t.}$ The

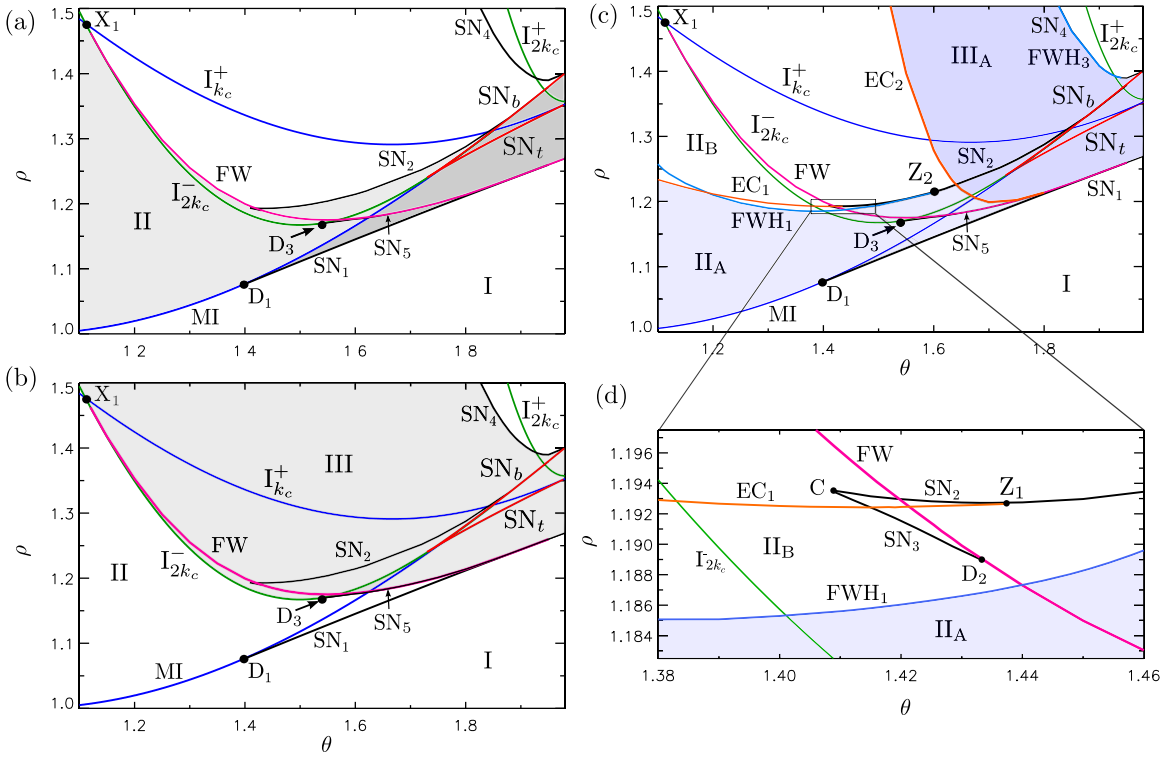

FIG. 6. Phase diagram in the (θ, ρ) parameter space showing the main bifurcations of the HSS and pattern states. In (a),(b) the regions of existence of P_{k_c} and P_{2k_c} are shaded in light gray. In (a) the region of bistability between A_0^b and P_{k_c} is indicated in dark gray. For clarity the bifurcation lines EC and FWH corresponding to the Eckhaus and Hopf bifurcations are omitted in these two panels. Panel (c) shows the full phase diagram, including the EC and FWH lines, with the region of stability of both patterns shown in light blue. Panel (d) shows a close-up view of (c) around the cusp bifurcation C. The symbol • represents the codimension-two points X_1, C, D_1, D_2, and D_3, Z_1, and Z_2.

complex amplitudes z_1, z_2 then satisfy the equations [25–27]

$$\dot{z}_1 = \alpha z_1 + c_1 \bar{z}_1 z_2 + (e_{11}|z_1|^2 + e_{12}|z_2|^2) z_1 + \cdots ,$$
$$\dot{z}_2 = (\alpha - \beta) z_2 + c_2 z_1^2 + (e_{21}|z_1|^2 + e_{22}|z_2|^2) z_2 + \cdots . \tag{23}$$

We see that for fixed $\beta > 0$ the HSS solution $(z_1, z_2) = (0, 0)$ loses stability in succession to modes with wave numbers k_c, $2k_c$ as α increases. We also see that the equations admit a pure P_{2k_c} solution $(0, z_2)$ but that the P_{k_c} state acquires a contribution with wave number $2k_c$ as soon as $\alpha > 0$, exactly as observed in the figure, i.e., the mode starting out as $(z_1, 0)$ is in fact a mixed mode (z_1, z_2) as soon as $\alpha > 0$. Moreover, as α increases the contribution from the amplitude z_2 grows and the mixed mode terminates on the $(0, z_2)$ branch of pure wave number $2k_c$ states, also as observed. The latter is a 2:1 resonance since at this bifurcation a pure mode with wave number $2k_c$ bifurcates into a mixed mode with a contribution from wave number k_c. We can therefore think of this bifurcation as a subharmonic instability in space.

In the next section, we explore how the bifurcation structure connecting P_{k_c} with all its harmonics is modified when the cavity detuning θ varies.

V. PATTERNS IN THE (θ, ρ) PLANE

Figure 6 shows the different bifurcation lines and dynamical regions introduced in the previous sections in the (θ, ρ) parameter space. For clarity we show three different versions of the phase diagram, with increasing complexity going from panel (a) to (c). Diagrams (a),(b) show the same diagram as in Fig. 3 together with the saddle nodes of pattern branches P_{k_c} and P_{2k_c} and the FW bifurcation that connects them. In (a) we shaded in light gray the region of existence of P_{k_c}, while in (b) we show the region of existence of P_{2k_c}. Looking at these two diagrams one can see a region of coexistence of both patterns, indicating the complex multistable nature of the system. The stability of the pattern states changes not only through saddle-node bifurcations, but also through subsequent Eckhaus (EC) and finite-wavelength-Hopf (FWH) instabilities, resulting in yet more complex scenarios. These new bifurcation lines are added in Figs. 6(c) and 6(d), with the latter a close-up view of panel (c). The aim of this section is to describe the different bifurcation lines and the dynamical regions shown in these phase diagrams, while Sec. VI discusses the stability of the patterns in greater detail. As this phase diagram is quite dense and therefore difficult to interpret, we also show (Fig. 7) how the bifurcation structure changes as a function of the pump ρ for increasing values of the detuning θ.

For small values of θ [Fig. 7(a), $\theta = 1.1 < 41/30$], the pattern P_{k_c} (red line) bifurcates supercritically from MI at $I_0 = I_c$ and connects back to the HSS at $I_{k_c}^+$; P_{2k_c} (blue line) is disconnected from P_{k_c} and bifurcates from $I_{2k_c}^-$ and then extends to higher values of ρ before connecting with HSS at $I_{2k_c}^+$. At this parameter value both patterns emerge supercritically from HSS, with P_{k_c} stable and P_{2k_c} initially

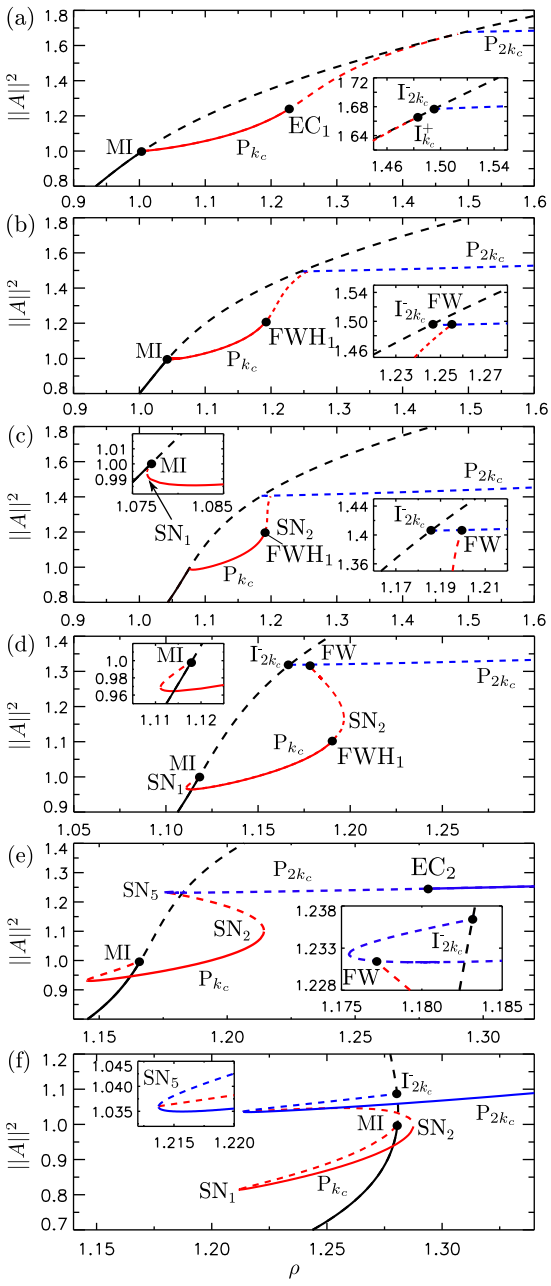

FIG. 7. Bifurcation diagrams corresponding to (a) $\theta = 1.1$, (b) $\theta = 1.3$, (c) $\theta = 1.4$, (d) $\theta = 1.5$, (e) $\theta = 1.6$, and (f) $\theta = 1.8$. Red lines correspond to P_{k_c} and the blue lines to P_{2k_c}. Panels (a) and (b) show the situation before and after the codimension-two point X_1. Panels (b) and (c) show the transition from supercritical to subcritical bifurcation of pattern P_{k_c} via a degenerate HH at $\theta = 41/30$. For $\theta = 1.5$ [panel (d)] P_{2k_c} bifurcates supercritically from HSS at $I^-_{2k_c}$. In contrast, for $\theta = 1.6$ [panel (e)] P_{2k_c} emerges subcritically. Solid (dashed) lines indicate stable (unstable) branches.

unstable. However, both states can change stability through subsequent Eckhaus (EC) and finite-wavelength-Hopf (FWH) instabilities [see Fig. 6(c)]. In particular, for $\theta = 1.1$, P_{k_c} becomes unstable at the EC_1 point. When θ increases, $I^+_{k_c}$ and $I^-_{2k_c}$ collide at a codimension-two bifurcation labeled X_1, after which the P_{k_c} and P_{2k_c} branches connect to one another via a FW instability originating in X_1. This is the 2:1 spatial resonance mentioned in the previous section. This situation is shown in Fig. 7(b). Note that P_{k_c} now loses stability through the FWH_1 bifurcation.

At $\theta = 41/30$, the bifurcation to P_{k_c} is a degenerate HH bifurcation denoted in Figs. 6(a)–6(c) by D_1. For $\theta > 41/30$ the bifurcation is subcritical as shown in Fig. 7(c) for $\theta = 1.4$. Here, P_{k_c} is initially unstable but acquires stability at a saddle-node labeled SN_1. This branch subsequently loses stability at FWH_1 and connects with P_{2k_c} at FW just as in Fig. 7(b). It follows that in this regime there is a small region of coexistence between stable A_0^b and stable P_{k_c}, close to MI. As a result localized structures (LS) are also present and these are organized in a so-called homoclinic snaking structure [20,28–31]. The A_0^b–P_{k_c} bistability region is colored in dark gray in Fig. 6(a). For slightly larger values of θ a cusp (C) bifurcation is encountered creating a pair of saddle nodes SN_2 and SN_3 on the P_{k_c} branch [see Fig. 6(d)]. The SN_3 disappears almost immediately in a degenerate codimension-two point D_2 on the curve FW, changing the direction of branching of P_{k_c} from P_{2k_c}, while the EC_1 bifurcation collides with SN_2 and disappears in another codimension-two point (Z_1). The pattern P_{k_c} bifurcates supercritically from FW below the D_2 point and subcritically above it. The latter case is shown in Fig. 7(d) for $\theta = 1.5$. Here the upper portion of the P_{k_c} branch is stable between SN_1 and FWH_1, and unstable otherwise. Further increase in θ leads to a collision of FWH_1 with SN_2 and its disappearance in a codimension-two point Z_2. After this point the P_{k_c} branch is stable between SN_1 and SN_2.

For $\theta = 1.6$ [Fig. 7(e)], the HSS branch is still monotonic but P_{2k_c} now also emerges subcritically, having crossed another degeneracy at D_3 (Fig. 6). This leads to the creation of a saddle-node bifurcation SN_5 on the P_{2k_c} branch similar to SN_1 on the P_{k_c} branch. At the same time an Eckhaus (EC_2) bifurcation moves in from larger values of ρ, stabilizing the large ρ part of the P_{2k_c} branch. With further increase in θ the EC_2 point collides with FW, and the whole P_{2k_c} branch beyond FW becomes stable. For yet larger θ the FW point moves towards SN_5 so that P_{k_c} now terminates on P_{2k_c} at SN_5 and the P_{2k_c} branch is stable from SN_5 towards larger ρ. This multiple bifurcation occurs for $\theta \approx 1.72$ but is not analyzed in this work. Figure 7(f) shows the resulting bifurcation diagram when $\theta = 1.8$. Since this value of θ exceeds $\sqrt{3}$ the HSS branch is no longer monotone, with $I^-_{k_c}$ lying below the resulting fold SN_b and $I^-_{2k_c}$ above it. The regions of stability of P_{k_c} and P_{2k_c} are shaded using light gray in Figs. 6(c) and 6(d).

In Figs. 6 and 7, we focus on the bifurcations associated with P_{k_c} and P_{2k_c}, although very similar transitions occur between P_{2k_c} and P_{4k_c}, P_{4k_c} and P_{8k_c}, and so on. This scenario resembles foliated snaking of localized structures that appears for $\theta > 2$ [20]. Since $k_c \to 0$ as $\theta \to 2$ from below, in a finite system a pattern with domain-size wavelength becomes indistinguishable from a single peak localized structure present for $\theta > 2$, i.e., in the limit $\theta \to 2$ P_{k_c} becomes a single peak LS, P_{2k_c} becomes a two peak LS, etc., thereby reproducing precisely the foliated snaking bifurcation scenario.

A similar pattern organization exists for patterns with wave number $k \neq k_c$, implying that the complete scenario is fundamentally complex. A detailed study of secondary bifurcations

of patterns with wave numbers $k \neq k_c$ is therefore left for future work.

VI. LINEAR STABILITY ANALYSIS OF THE PATTERN SOLUTIONS

The preceding section has highlighted the importance of secondary bifurcations such as the finite wavelength (FW) and finite-wavelength-Hopf (FWH) bifurcations, as well as the wavelength changing instability called the Eckhaus instability. Long wavelength secondary instabilities of one-dimensional patterns can be classified using symmetry-based arguments that describe the possible coupling between the instability modes and the phase of the periodic pattern solution [32]. This procedure is particularly valuable in the case of the Eckhaus instability which is a long wavelength instability, with domain-size wavelength. The nonlinear evolution of this instability generally leads to the generation of a phase slip whereby a new roll is injected (or annihilated) at the location of the phase slip, followed by relaxation of the new pattern towards a periodic structure with a new and different wavelength in the domain [33,34]. This process cannot be described by a phase equation which necessarily breaks down prior to a phase slip.

The traditional approach to describing the Eckhaus instability is based on the use of an amplitude equation, the Ginzburg-Landau equation, that describes the pattern-forming instability close to the primary pattern-forming bifurcation, assumed to be supercritical [34,35]. As a result the predictions concerning the onset and evolution of the Eckhaus instability are valid only when the instability sets are close to the primary instability. We have seen that in the present case this is not the case; moreover, in some cases the primary bifurcation is subcritical and the analysis of the Eckhaus instability is then substantially modified [36]. For this reason we apply here a technique described in [7,37] that permits us to compute the onset of the Eckhaus instability for finite amplitude fully nonlinear spatially periodic patterns. The technique is necessarily numerical but allows us to find and characterize, as a function of θ, ρ, and k, the secondary bifurcations introduced in Sec. V. Similar numerical studies have been performed in the context of fluid mechanics in Ref. [38] and for supercritical patterns within the LLE in Ref. [21].

The stationary patterns, hereafter $A_p = (U_p, V_p)$, can be written as a Fourier modal expansion

$$A_p(x) = \sum_{m=-N/2+1}^{N/2} a_m e^{imkx}, \tag{24}$$

with k the wave number of the pattern, a_m the complex amplitude of the Fourier mode with wave number mk, and N the number of Fourier modes retained in the analysis. To study the linear stability of such a pattern state, one must first linearize Eq. (1) around the state (24). Writing $A(x,t) = A_p(x) + \epsilon\delta A(x,t)$, $\epsilon \ll 1$, leads to the following leading order equation for the perturbation δA:

$$\partial_t \delta A = -(1+i\theta)\delta A + i\partial_x^2 \delta A + 2i|A_p|^2\delta A + iA_p^2\delta A^*. \tag{25}$$

Owing to the periodicity of A_p, we can apply the Bloch ansatz and write the eigenmodes of this equation as Bloch waves [32]

$$\delta A(x,t) = e^{iqx}\delta a(x,t,q) + e^{-iqx}\delta a(x,t,-q), \tag{26}$$

where δa has the same spatial period as the pattern A_p and can be written in the form

$$\delta a(x,t,q) = \sum_{m=-N/2+1}^{N/2} \delta a_m(t,q)e^{ikmx}. \tag{27}$$

Inserting Eqs. (24) and (26) in Eq. (25) leads to a set of linear equations for the complex amplitudes $\delta a_n^{\pm} \equiv \delta a_n(t, \pm q)$, namely

$$\frac{d}{dt}\delta a_n^{\pm} = -(1+i\theta)\delta a_n^{\pm} - i(kn \pm q)^2\delta a_n^{\pm} + i\sum_{m=-N/2+1}^{N/2} a_l a_m^* \delta a_{n-l+m}^{\pm} + i\sum_{m=-N/2+1}^{N/2} a_l a_m \delta a_{-n+l+m}^{*\pm}. \tag{28}$$

This equation has the form

$$\partial_t \Sigma(t,q) = L(a_n,q)\Sigma(t,q), \tag{29}$$

where

$$\Sigma(t,q) \equiv (\delta a_0^+, \ldots, \delta a_{N-1}^+, \delta a_0^{*-}, \ldots, \delta a_{N-1}^{*-}).$$

Thus the linear stability analysis of $A_p(x)$ reduces to finding the 2N eigenvalues $\lambda_j(q)$ of the $N \times N$ matrix $L(a_n, q)$ and the corresponding eigenvectors, for each value of q. For more details, see Refs. [7,37,39]. The eigenvalues for a given q determine the stability of the pattern against perturbations containing wave numbers $k \pm q$ for any k. For this purpose it is sufficient to consider only q values inside the first Brillouin zone. Any perturbation with wave number q' outside the Brillouin zone is equivalent to another with $q = q' + k$. In solid state physics this representation is described as the *reduced zone scheme* [40].

Using this technique we characterize how the eigenspectrum of $L(a_n, q)$ changes as a function of q for different values of (θ, ρ), and predict the different secondary bifurcations that a pattern with wave number k undergoes.

Figure 8 shows an enlarged version of the phase diagram in Fig. 6. Both P_{k_c} and P_{2k_c} change their stability across the lines EC (Eckhaus) and FWH (finite wavelength Hopf), as indicated in Figs. 6 and 8. Furthermore, their branches connect one another through the FW (finite wavelength) instability. For $\theta < 41/30$ P_{k_c} is initially stable and loses stability when crossing either EC_1 or FWH_1. For $\theta > 41/30$ P_{k_c} bifurcates subcritically and so is stable only between SN_1 and the lines EC_1 or FWH_1. In either case, P_{2k_c} is initially unstable but gains stability with increased detuning via EC_2 or FWH_2.

These bifurcations divide regions II and III (see Figs. 6 and 8) into the following subregions.

Region II_A: the pattern P_{k_c} is stable. This region spans the parameter space between MI and SN_1 from below, and EC_1, FWH_1, and SN_2 from above.

Region II_B: the pattern P_{k_c} is either Eckhaus unstable (by crossing EC_1) or Hopf unstable (by crossing FWH_1). This

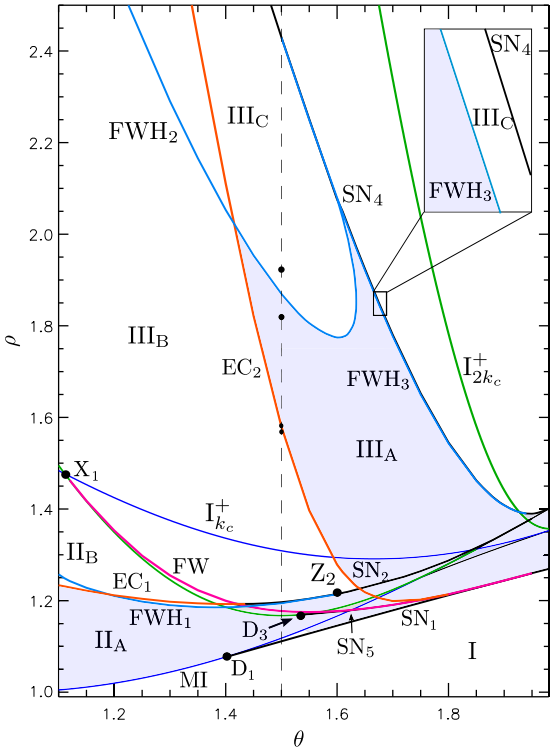

FIG. 8. Phase diagram in (θ, ρ) parameter space showing an enlargement of the diagrams shown in Fig. 6 focusing on the main stability regions of P_{k_c} labeled $II_{A,B}$ and P_{2k_c} labeled $III_{A,...,C}$. The dashed line at $\theta = 1.5$ refers to the slice of this diagram shown in Fig. 9. The small black dots along this line correspond to points where the stability analysis of the patterns shown in Sec. V was performed. In light blue we show the regions where P_{k_c} and P_{2k_c} are stable.

region spans the parameter space between EC_1 and FWH_1 from below and FW and SN_2 from above.

Region III_A: P_{2k_c} is stable between EC_2 and SN_5 from below and FWH_2 and FWH_3 from above.

Region III_B: the pattern P_{2k_c} is Eckhaus unstable. This region spans the parameter space between $I^-_{2k_c}$ and SN_5 from below and FWH_2 and EC_2 from above.

Region III_C: P_{2k_c} oscillates in time and in space. This region spans the parameter space inside the region defined by FWH_2 and FWH_3 from below and between FWH_3 and SN_4 (see inset).

In what follows we analyze in detail the different secondary bifurcations the periodic patterns undergo when the control parameters are varied. Without loss of generality, we focus on the P_{2k_c} branch, which—in addition to EC_2 and $FWH_{2,3}$—also undergoes an FW instability. This bifurcation is essential for its reconnection with the P_{k_c} branch. The dynamics of the latter when crossing EC_1 and FWH_1 are similar to those shown here for P_{2k_c}.

In Fig. 9, we show the bifurcation diagram for $\theta = 1.5$, a value we will use to explore the different instabilities in more detail. For $\theta = 1.6$, discussed in Sec. VI, the results are similar except that P_{2k_c} bifurcates initially subcritically. The temporal evolution indicated by arrows in the figure results from phase slips, as discussed next, and is obtained on a periodic domain of length $L = 2\pi n/k_c$, with $n = 16$.

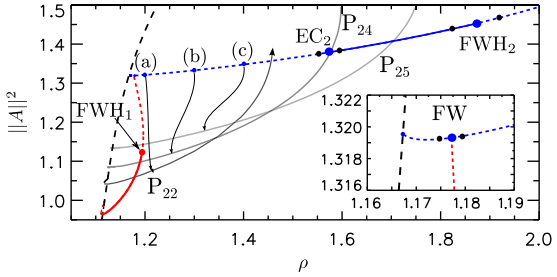

FIG. 9. Bifurcation diagram for $\theta = 1.5$. The pattern branch P_{k_c} (red) bifurcates subcritically from HSS at $I^-_{k_c}$, while the branch P_{2k_c} (blue) bifurcates supercritically at $I^-_{2k_c}$. Labels (a)–(c) correspond to the unstable patterns with 32 rolls initially that evolve in time to patterns with different numbers of rolls depending on the value of ρ and lying on new branches of periodic states (gray) labeled by P_n, where n is the new roll number. The points where linear stability analysis has been carried out are indicated using the symbol •.

A. Eckhaus instability

For values of θ and ρ in region III_B (see Fig. 8), patterns are unstable against long-wavelength perturbations ($q \sim 0$), and for this reason the Eckhaus instability is also known as a long-wavelength (LW) instability [11,41]. Furthermore, this instability is triggered by a phase instability [41]. For small values of q, the least stable branch of eigenvalues $\lambda_1(q)$ has a parabolic shape centered at $q = 0$, namely $\mathrm{Re}[\lambda_1(q)] \propto |q|^2$, and the instability takes place when the convexity of this eigenvalue branch changes sign.

The result of the stability analysis of P_{2k_c} for $\theta = 1.5$ and increasing values of ρ as one crosses the EC_2 instability threshold is summarized in Fig. 10. In panel (c) $\rho = 1.59$ and $\mathrm{Re}[\lambda_1(q)]$ is negative for all nonzero q. Therefore, P_{2k_c} is stable no matter the wavelength of the perturbation. This situation corresponds to region III_A in Fig. 8. In panel (b) $\rho = 1.58$ and the eigenspectrum flattens around $\mathrm{Re}[\lambda_1(q)] = 0$, indicating the onset of the EC instability. Finally, in panel (a) $\rho = 1.57$ and the eigenspectrum has changed its convexity, indicating that the pattern is now unstable to perturbations with $q \in [0, q^*]$. This property characterizes region III_B, which extends from EC_2 down to $I^-_{2k_c}$ as ρ decreases.

In Fig. 11 the right panels show the temporal evolution of an unstable initial condition along the branch P_{2k_c} together with the real part of the leading eigenvalue $\lambda_1(q)$ (left panels) for different values of ρ in region III_B. The labels (a)–(c)

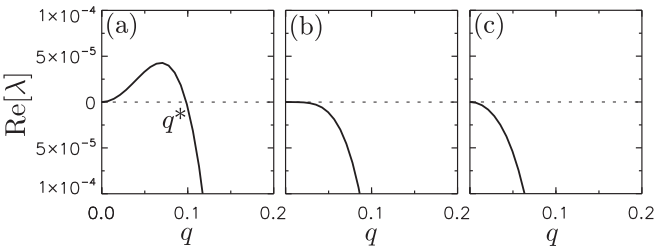

FIG. 10. Eigenspectrum in the vicinity of the EC instability of the P_{2k_c} branch when $\theta = 1.5$, showing $\mathrm{Re}[\lambda_1(q)]$ for different values of ρ: (a) $\rho = 1.57$, (b) $\rho = \rho_{EC_2} = 1.58$, and (c) $\rho = 1.59$.

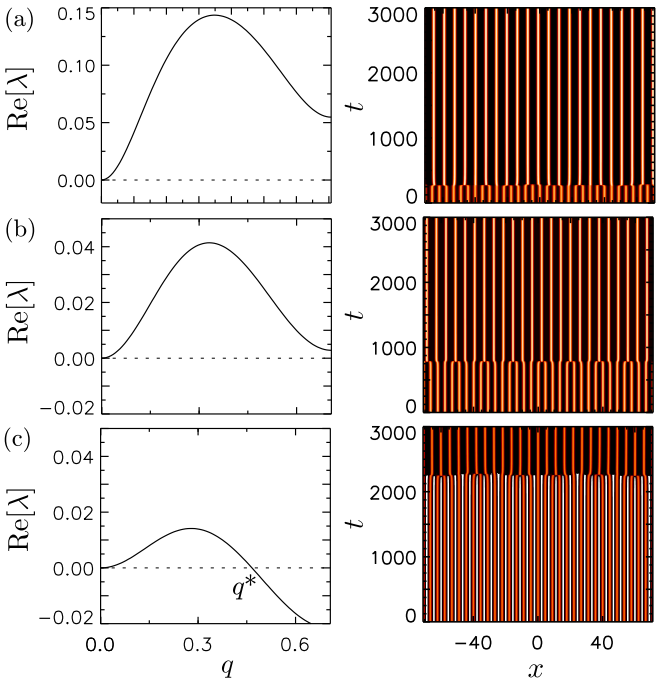

FIG. 11. Re[$\lambda_1(q)$] at $\theta = 1.5$ in the region of Eckhaus instability and the associated temporal evolution of an unstable initial pattern to patterns of different wavelengths. These new states are shown in gray in Fig. 9: an unstable pattern with initially 32 rolls evolves to P_{25} in panel (c) for $\rho = 1.4$, to P_{24} in panel (b) for $\rho = 1.3$, and to P_{22} in panel (a) for $\rho = 1.2$. The left panels show the unstable modes $0 < q < q^*$, while the right panels describe the resulting evolution in space-time plots.

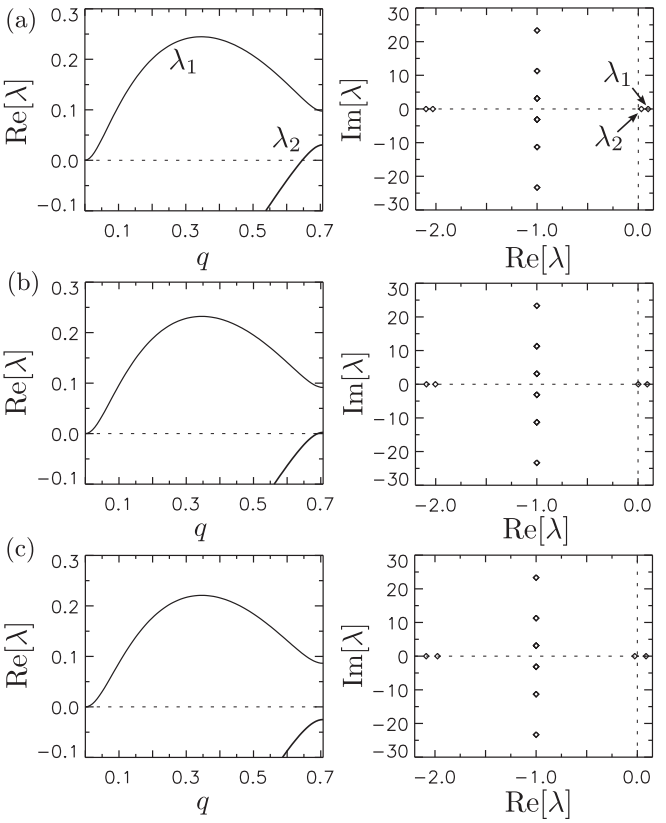

FIG. 12. Eigenspectrum of P_{2k_c} in the vicinity of the FW instability when $\theta = 1.5$, showing the first two branches Re[$\lambda_1(q)$] and Re[$\lambda_2(q)$] for different values of ρ: (a) $\rho = 1.175$, (b) $\rho = \rho_{FW} \approx 1.177$, and (c) $\rho = 1.179$.

correspond to different points along the branch P_{2k_c} identified in Fig. 9.

For $\rho = 1.4$ [Fig. 11(c)], P_{2k_c} is unstable to perturbations with q in between zero and q^*, and the most unstable mode is that corresponding to maximum growth rate. Time simulations show that after an initial transient during which the pattern appears stable, the wavelength of the pattern suddenly increases to the wavelength of the most unstable mode. The pattern, which initially had 32 rolls, becomes a pattern with 25 rolls that we label P_{25}. This new pattern can be tracked in ρ and results in the P_{25} solution branch plotted in Fig. 9.

Reducing the value of ρ further, the P_{2k_c} pattern becomes unstable to any $q \in [0, k'/2]$, with $k' = k_c/2$, and the most unstable wave number increases [Figs. 11(a) and 11(b)]. The maximum growth rate Re[$\lambda_1(q)$] also increases so that the time needed to destabilize the pattern decreases with ρ. The final patterns that are reached further beyond the EC_2 instability are P_{24} with 24 peaks in case (b) and the pattern P_{22} in case (a). Once tracked in ρ, these stationary patterns generate the solution branches shown in Fig. 9.

B. Finite-wavelength instability

We now characterize the finite-wavelength (FW) instability that allows the pattern P_{k_c} to terminate on P_{2k_c}. As already mentioned these locations correspond to a spatial 2:1 resonance located along the line FW in Fig. 8. However, the theory described in Refs. [25–27] applies only near the codimension-two case in which the two primary bifurcations from HSS to states with wave numbers k_c and $2k_c$ occur in close succession. This is not the case here, and we therefore employ the numerical technique of the previous section to compute the location of the FW bifurcation when this occurs in the fully nonlinear regime.

If $k' = 2k_c$ is the wave number of P_{2k_c}, the FW bifurcation is characterized by a branch of eigenvalues $\lambda_2(q)$ having a parabolic shape centered at $q = k'/2$, i.e., Re[$\lambda_2(q)$] $\propto |q - k'/2|^2$, which crosses Re[$\lambda_2(q)$] $= 0$ at $q = k'/2$. This transition is shown in Fig. 12 for $\theta = 1.5$ and for three values of ρ in the vicinity of the FW bifurcation (see inset in Fig. 9). The real part of the two leading eigenvalues $\lambda_1(q)$ and $\lambda_2(q)$ is shown in the left panels, while the right columns show the full eigenspectrum at $q = k'/2 = k_c$. In any case Re[$\lambda_1(q)$] is positive for all the range $q \in [0, k'/2 = k_c]$, and therefore P_{2k_c} is unstable against Bloch modes with $q \in [0, k_c]$, i.e., in this regime P_{2k_c} is EC unstable. The FW transition is triggered by the second eigenvalue λ_2 centered at $q = k'/2$. In (a) $\rho < \rho_{FW}$, and a portion of the branch Re[$\lambda_2(q)$] is positive, with its maximum occurring at $q = k'/2$. Therefore, in this case P_{2k_c} is unstable to the most unstable mode, i.e., $q = k'/2 = k_c$, and therefore to P_{k_c}, in addition to the unstable EC mode. In (b) $\rho = \rho_{FW}$, and the maximum growth rate Re[$\lambda_2(q)$] at $q = k'/2$ vanishes, as can be appreciated by looking at the corresponding eigenspectrum in the right column. This point therefore corresponds to the presence of the FW bifurcation.

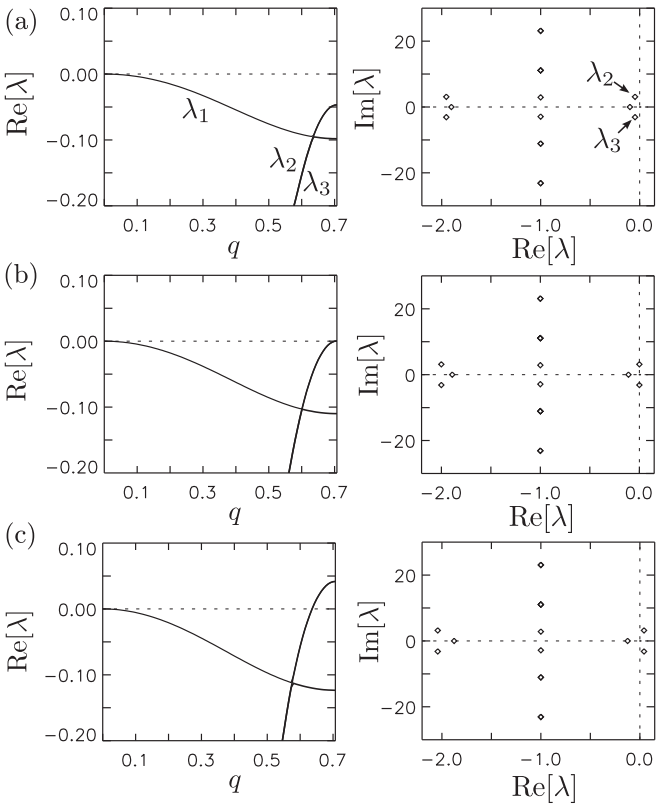

FIG. 13. Hopf bifurcation of P_{2k_c} at $\theta = 1.5$ showing (left panels) Re[$\lambda(q)$] for different values of ρ: (a) $\rho = 1.82$, (b) $\rho = \rho_{\rm FWH} = 1.87$, and (c) $\rho = 1.92$. The right panels show the corresponding eigenspectrum at $q = k_c$, the onset wave number.

Finally, panel (c) shows the situation at $\rho > \rho_{\rm FW}$, where Re[$\lambda_2(q)$] is negative for all q, and the P_{2k_c} pattern is FW stable.

C. Finite-wavelength-Hopf instability

For values of θ and ρ in region $\rm III_C$ patterns undergo a finite-wavelength-Hopf instability, hereafter FWH. In contrast to the homogeneous Hopf bifurcation which occurs with $q = 0$, this Hopf bifurcation sets in with a finite wave number $q \neq 0$, here $q = k_c$. In the former case, patterns which are Hopf unstable will oscillate with a uniform amplitude and temporal period $T = 2\pi/\omega$, with $\omega = \mathrm{Im}(\lambda_2(0)) = \mathrm{Im}(\lambda_3(0))$. Here $\lambda_{2,3}(0)$ are the Hopf modes. In the FWH case, however, patterns oscillate both in time and in space, and this is why this instability is also referred to as a *wave instability* (WI) [11,41–44].

In Fig. 13 the real part of the three leading eigenvalues (left) and the full eigenspectrum at $q = k'/2 = k_c$ (right) are plotted when crossing the $\rm FWH_2$ bifurcation at $\theta = 1.5$ (see Figs. 8 and 9). In panel (a) $\rho = 1.82$, and the real parts of $\lambda_2(q)$ and $\lambda_3(q)$ are both negative, with a parabolic shape centered at $q = k'/2 = k_c$. In fact these eigenvalues are complex conjugates of one another, as can be seen in the full eigenspectrum for $q = k_c$ shown in the right panel. This is the situation in region $\rm III_A$, where P_{2k_c} is FWH stable. In panel (b) $\rho = \rho_{\rm FWH_2} = 1.87$ and the real part of the complex conjugate eigenvalues $\lambda_{2,3}(q)$ vanishes at $q = k_c$, indicating the onset of the $\rm FWH_2$ bifurcation. Finally, in (c) $\rho = 1.92$, and the real part of the eigenvalues is now positive and P_{2k_c} starts to oscillate, not only in time but also in space. This is the situation of region $\rm III_C$ shown in Fig. 8.

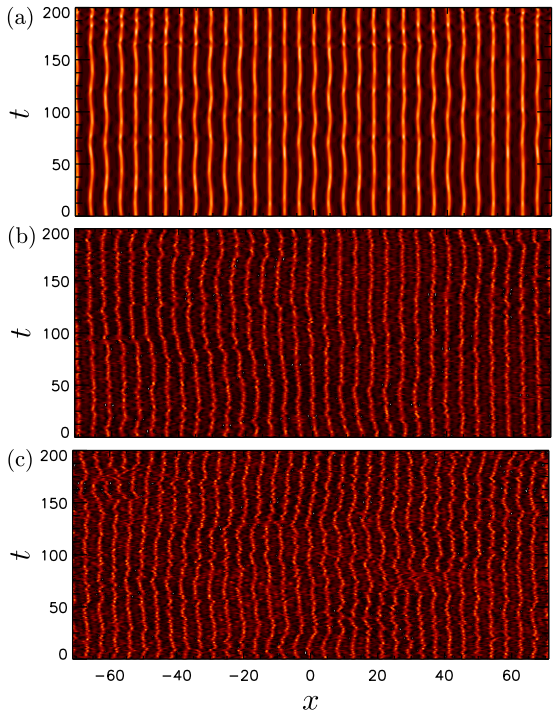

FIG. 14. Time evolution of the oscillating patterns for $\theta = 1.5$ and (a) $\rho = 1.9$, (b) $\rho = 2.1$, and (c) $\rho = 2.3$.

In Fig. 14, we show the resulting oscillatory states for different values of ρ in region $\rm III_C$ when $\theta = 1.5$. For $\rho = 1.9$ [see panel (i)], the amplitude of P_{2k_c} oscillates nonuniformly not only in time but also in space resulting in zigzag motion whose amplitude grows with increasing ρ as seen in panel (b). Finally, in panel (c), for $\rho = 2.4$, the pattern exhibits much complex dynamics including phase slips at which peaks merge or split resulting in fluctuations in the total number $n(t)$ of rolls in the domain at any one time. A complete description and understanding of the dynamics of these oscillatory states in time and space involves interaction with the marginally stable $q = 0$ mode (Fig. 13 and [45]) and is beyond the scope of this paper.

VII. CONCLUSIONS

In this paper we have studied the bifurcation structure and stability properties of spatially periodic patterns arising in the LL model in the anomalous GVD dispersion regime.

Linear stability theory predicts that the HSS solution becomes modulationally unstable at $I_0 = I_c = 1$ to a pattern with a critical wave number $k_c = \sqrt{2-\theta}$, namely P_{k_c} [1,5]. A weakly nonlinear analysis has allowed us to obtain a perturbative description of this pattern in the neighborhood of this bifurcation. From this calculation one finds that P_{k_c} emerges supercritically for $\theta < 41/30$ and subcritically when $\theta > 41/30$, where $\theta = 41/30$ corresponds to a degenerate HH point.

This analytical approximation for the pattern P_{k_c} around the MI point (or, equivalently, HH) has been used as an initial condition in a numerical continuation algorithm that allowed us to track the pattern solutions to parameter values away from the bifurcation point. Using this method, we have studied the bifurcation structure of spatially periodic patterns as a function of ρ for different values of the detuning θ. In doing so, we have found that for low θ patterns arising from the MI bifurcation reconnect with the HSS for larger values of the intracavity intensity I_0, at $I^+_{k_c}$. In addition, harmonic patterns with wave numbers nk_c, $n = 2, 4, \ldots$, also bifurcate from the HSS, P_{2k_c} at $I^{\pm}_{2k_c}$, P_{4k_c} at $I^{\pm}_{4k_c}$, etc. With increasing θ these two types of patterns connect pairwise in a 2:1 spatial resonance, for example, P_{k_c} with P_{2k_c} and P_{2k_c} with P_{4k_c}. We have referred to these bifurcation points as finite-wavelength (FW) instabilities and computed their location via numerical Floquet analysis. This FW bifurcation originates in the codimension-two point X, which appears to organize these connections. Finally, as $\theta \to 2$ and $k_c \to 0$ the bifurcation structure of the patterns transforms into foliated snaking of localized structures [20], as a pattern with infinite wavelength corresponds in effect to a single peak localized structure in a finite size system.

We have provided an almost complete discussion of the various possible secondary bifurcations in the parameter space (θ, ρ) of the LL equation, mapping out the different dynamical regions for the patterns P_{k_c} and P_{2k_c}. In particular, patterns corresponding to P_{2k_c} were found to undergo Eckhaus and finite-wavelength-Hopf instabilities, in addition to the FW instability, and these were found to lead to rich and complex dynamics. Several significant but higher codimension bifurcations were also identified, but a detailed study of these remains for future work.

While we have focused our study on patterns with the critical wave number k_c determined by the onset of the MI, and its harmonics, we have confirmed that similar behavior also occurs for patterns with wave number $k \neq k_c$ that also emerge from the HSS solution but do so for $I_0 > I_c$. Together with the instabilities described in this work, other bifurcations such as an FW with $q = k/3$ are also known to exist [21]. A detailed study of secondary instabilities of patterns with arbitrary wave number k is beyond the scope of this paper, however, and is likewise left to future work.

ACKNOWLEDGMENTS

We acknowledge support from the Research Foundation–Flanders (FWO-Vlaanderen) (P.P.R.), internal Funds from KU Leuven (P.P.R.), the Belgian Science Policy Office (BelSPO) under Grant No. IAP 7-35, the Research Council of the Vrije Universiteit Brussel, the Agencia Estatal de Investigación (AEI, Spain) and Fondo Europeo de Desarrollo Regional under Project ESoTECoS, Grant No. FIS2015-63628-C2-1-R (AEI/FEDER,UE) (D.G.), as well as the National Science Foundation under Grant No. DMS-1613132 (E.K.).

[1] L. A. Lugiato and R. Lefever, Spatial Dissipative Structures in Passive Optical Systems, Phys. Rev. Lett. **58**, 2209 (1987).

[2] W. J. Firth, A. J. Scroggie, G. S. McDonald, and L. A. Lugiato, Hexagonal patterns in optical bistability, Phys. Rev. A **46**, R3609 (1992).

[3] W. J. Firth and G. K. Harkness, Cavity solitons, Asian J. Phys. **7**, 665 (1998).

[4] A. J. Scroggie, W. J. Firth, G. S. McDonald, M. Tlidi, R. Lefever, and L. A. Lugiato, Pattern formation in a passive Kerr cavity, Chaos Solitons Fractals **4**, 1323 (1994).

[5] M. Tlidi, R. Lefever, and P. Mandel, Pattern selection in optical bistability, Quantum Semiclass. Opt. **8**, 931 (1996).

[6] M. Haelterman, S. Trillo, and S. Wabnitz, Dissipative modulation instability in a nonlinear dispersive ring cavity, Opt. Commun. **91**, 401 (1992).

[7] D. Gomila and P. Colet, Transition from hexagons to optical turbulence, Phys. Rev. A **68**, 011801(R) (2003); Dynamics of hexagonal patterns in a self-focusing Kerr cavity, Phys. Rev. E **76**, 016217 (2007).

[8] R. Kapral and K. Showalter, *Chemical Waves and Patterns* (Kluwer, Dordrecht, 1995).

[9] A. M. Turing, The chemical basis of morphogenesis, Philos. Trans. R. Soc. B **237**, 37 (1952).

[10] V. Castets, E. Dulos, J. Boissonade, and P. De Kepper, Experimental Evidence of a Sustained Standing Turing-Type Nonequilibrium Chemical Pattern, Phys. Rev. Lett. **64**, 2953 (1990).

[11] M. C. Cross and P. C. Hohenberg, Pattern-formation outside of equilibrium, Rev. Mod. Phys. **65**, 851 (1993).

[12] S. Coen, H. G. Randle, T. Sylvestre, and M. Erkintalo, Modeling of octave-spanning Kerr frequency combs using a generalized mean-field Lugiato-Lefever model, Opt. Lett. **38**, 37 (2013).

[13] Y. K. Chembo and C. R. Menyuk, Spatiotemporal Lugiato-Lefever formalism for Kerr-comb generation in whispering-gallery-mode resonators, Phys. Rev. A **87**, 053852 (2013).

[14] F. Leo, S. Coen, P. Kockaert, S.-P. Gorza, P. Emplit, and M. Haelterman, Temporal cavity solitons in one-dimensional Kerr media as bits in an all-optical buffer, Nat. Photon. **4**, 471 (2010).

[15] T. Herr, K. Hartinger, J. Riemensberger, C. Y. Wang, E. Gavartin, R. Holzwarth, M. L. Gorodetsky, and T. J. Kippenberg, Universal formation dynamics and noise of Kerr-frequency combs in microresonators, Nat. Photon. **6**, 480 (2012).

[16] F. Leo, L. Gelens, P. Emplit, M. Haelterman, and S. Coen, Dynamics of one-dimensional Kerr cavity solitons, Opt. Exp. **21**, 9180 (2013).

[17] P. Parra-Rivas, D. Gomila, M. A. Matías, S. Coen, and L. Gelens, Dynamics of localized and patterned structures in the Lugiato-Lefever equation determine the stability and shape of optical frequency combs, Phys. Rev. A **89**, 043813 (2014).

[18] C. Godey, I. V. Balakireva, A. Coillet, and Y. K. Chembo, Stability analysis of the spatiotemporal Lugiato-Lefever model for Kerr optical frequency combs in the anomalous and normal dispersion regimes, Phys. Rev. A **89**, 063814 (2014).

[19] T. J. Kippenberg, R. Holzwarth, and S. A. Diddams, Microresonator-based optical frequency combs, Science **332**, 555 (2011).

[20] P. Parra-Rivas, D. Gomila, L. Gelens, and E. Knobloch, Bifurcation structure of localized states in the Lugiato-Lefever equation with anomalous dispersion, Phys. Rev. E **97**, 042204 (2018).

[21] N. Périnet, N. Verschueren, and S. Coulibaly, Eckhaus instability in the Lugiato-Lefever model, Eur. Phys. J. D **71**, 243 (2017).

[22] E. L. Allgower and K. Georg, *Numerical Continuation Methods: An Introduction* (Springer-Verlag, Berlin, 1990).

[23] H. B. Keller, *Lectures on Numerical Methods in Bifurcation Problems*, Tata Institute of Fundamental Research (Springer-Verlag, Berlin, 1986).

[24] H. D. Mittelmann, A pseudo-arclength continuation method for nonlinear eigenvalue problems, SIAM J. Numer. Anal. **23**, 1007 (1986).

[25] D. Armbruster, J. Guckenheimer, and P. Holmes, Heteroclinic cycles and modulated traveling waves in systems with O(2) symmetry, Phys. D (Amsterdam, Neth.) **29**, 257 (1988).

[26] M. R. E. Proctor and C. A. Jones, The interaction of two spatially resonant patterns in thermal convection. Part 1. Exact 2:1 resonance, J. Fluid Mech. **188**, 301 (1988).

[27] J. Porter and E. Knobloch, New type of complex dynamics in the 1:2 spatial resonance, Phys. D (Amsterdam, Neth.) **159**, 125 (2001).

[28] P. Coullet, C. Riera, and C. Tresser, Stable Static Localized Structures in One Dimension, Phys. Rev. Lett. **84**, 3069 (2000).

[29] D. Gomila, A. J. Scroggie, and W. J. Firth, Bifurcation structure for dissipative solitons, Phys. D (Amsterdam, Neth.) **227**, 70 (2007).

[30] P. D. Woods and A. R. Champneys, Heteroclinic tangles and homoclinic snaking in the unfolding of a degenerate reversible Hamiltonian-Hopf bifurcation, Phys. D (Amsterdam, Neth.) **129**, 147 (1999).

[31] J. Burke and E. Knobloch, Localized states in the generalized Swift-Hohenberg equation, Phys. Rev. E **73**, 056211 (2006).

[32] P. Coullet and G. Iooss, Instabilities of One-Dimensional Cellular Patterns, Phys. Rev. Lett. **64**, 866 (1990).

[33] L. Kramer and W. Zimmermann, On the Eckhaus instability for spatially periodic patterns, Phys. D (Amsterdam, Neth.) **16**, 221 (1985).

[34] L. S. Tuckerman and D. Barkley, Bifurcation analysis of the Eckhaus instability, Phys. D (Amsterdam, Neth.) **46**, 57 (1990).

[35] Z. Liu, F. Leo, S. Coulibaly, and M. Taki, Secondary instabilities in all fiber ring cavities, Phys. Rev. A **90**, 033837 (2014).

[36] H.-C. Kao and E. Knobloch, Weakly subcritical stationary patterns: Eckhaus instability and homoclinic snaking, Phys. Rev. E **85**, 026211 (2012).

[37] G. Harkness, G.-L. Oppo, R. Martin, A. J. Scroggie, and W. J. Firth, Elimination of spatiotemporal disorder by Fourier space techniques, Phys. Rev. A **58**, 2577 (1998).

[38] A. Bergeon, J. Burke, E. Knobloch and I. Mercader, Eckhaus instability and homoclinic snaking, Phys. Rev. E **78**, 046201 (2008).

[39] G. Harkness, W. J. Firth, G.-L. Oppo, and J. M. McSloy, Computationally determined existence and stability of transverse structures. I. Periodic optical patterns, Phys. Rev. E **66**, 046605 (2002).

[40] N. W. Ashcroft and N. Mermin, *Solid State Physics* (Harcourt College Publishers, New York, 1979).

[41] D. Walgraef, *Spatio-Temporal Pattern Formation* (Springer-Verlag, Berlin, 1997).

[42] M. Hildebrand, A. S. Mikhailov, and G. Ertl, Traveling Nanoscale Structures in Reactive Adsorbates with Attractive Lateral Interactions, Phys. Rev. Lett. **81**, 2602 (1998).

[43] A. M. Zhabotinsky, M. Dolnik, and I. R. Epstein, Pattern formation arising from wave instability in a simple reaction-diffusion system, J. Chem. Phys. **103**, 10306 (1995).

[44] M. Dolnik, A. M. Zhabotinsky, A. B. Rovinsky, and I. R. Epstein, Standing waves in a two-dimensional reaction-diffusion model with the short-wave instability, J. Phys. Chem. A **103**, 38 (1999); M. Dolnik, A. B. Rovinsky, A. M. Zhabotinsky, and I. R. Epstein, Spatio-temporal patterns in a reaction-diffusion system with wave instability, Chem. Eng. Sci. **55**, 223 (2000).

[45] S. M. Cox and P. C. Matthews, New instabilities in two-dimensional rotating convection and magnetoconvection, Phys. D (Amsterdam, Neth.) **149**, 210 (2001); D. M. Winterbottom, P. C. Matthews and S. M. Cox, Oscillatory pattern formation with a conserved quantity, Nonlinearity **18**, 1031 (2005).